INSTITUTE OF PHYSICS PUBLISHING NANOTECHNOLOGY
Nanotechnology **17** (2006) 5659–5668 doi:10.1088/0957-4484/17/22/021

Molecular transport in a crowded volume created from vertically aligned carbon nanofibres: a fluorescence recovery after photobleaching study

J D Fowlkes[1,2,3,5], E D Hullander[1,3], B L Fletcher[1,2,3], S T Retterer[1,2,3], A V Melechko[1,4], D K Hensley[1,4], M L Simpson[1,2,4] and M J Doktycz[1,3]

[1] Molecular-Scale Engineering and Nanoscale Technologies Research Group, Condensed Matter Sciences Division, Oak Ridge National Laboratory, PO Box 2008, Oak Ridge, TN 37831-6006, USA
[2] Materials Science and Engineering Department, The University of Tennessee, Knoxville, TN 37996-2200, USA
[3] Biological and Nanoscale Systems Group, Life Sciences Division, Oak Ridge National Laboratory, PO Box 2008, Oak Ridge, TN 37831-6123, USA
[4] Center for Nanophase Materials Sciences, Oak Ridge National Lab, PO Box 2008, Oak Ridge, TN 37831-6493, USA

E-mail: fo2@ornl.gov (J D Fowlkes)

Received 30 May 2006, in final form 25 September 2006
Published 30 October 2006
Online at stacks.iop.org/Nano/17/5659

Abstract
Rapid and selective molecular exchange across a barrier is essential for emulating the properties of biological membranes. Vertically-aligned carbon nanofibre (VACNF) forests have shown great promise as membrane mimics, owing to their mechanical stability, their ease of integration with microfabrication technologies and the ability to tailor their morphology and surface properties. However, quantifying transport through synthetic membranes having micro- and nanoscale features is challenging. Here, fluorescence recovery after photobleaching (FRAP) is coupled with finite difference and Monte Carlo simulations to quantify diffusive transport in microfluidic structures containing VACNF forests. Anomalous subdiffusion was observed for FITC (hydrodynamic radius of 0.54 nm) diffusion through both VACNFs and SiO_2-coated VACNFS (oxVACNFs). Anomalous subdiffusion can be attributed to multiple FITC–nanofibre interactions for the case of diffusion through the VACNF forest. Volume crowding was identified as the cause of anomalous subdiffusion in the oxVACNF forest. In both cases the diffusion mode changes to a time-independent, Fickian mode of transport that can be defined by a crossover length (R_{CR}). By identifying the space-and time-dependent transport characteristics of the VACNF forest, the dimensional features of membranes can be tailored to achieve predictable molecular exchange.

M Supplementary data files are available from stacks.iop.org/Nano/17/5659

[5] Author to whom any correspondence should be addressed.

1. Introduction

A synthetic membrane that emulates biological functions of its cellular model constitutes one of the major challenges for developing artificial biological cells. The lipid bilayer that constitutes biological membranes defines the cell volume and controls the exchange of materials. Yet, the lipid bilayer can be fragile and difficult to integrate with synthetic structures intended for biomedical applications. Synthetic membranes engineered with nanoscale materials offer a robust alternative. They approach the scale of biological membranes, but retain the ease of integration necessary for the broad application of such technologies.

We have been developing synthetic membranes comprised of a stochastic array, or forest, of VACNFs [1–4] with the goal of mimicking aspects of cell membrane function. In particular, we are interested in containing cellular scale volume reactions, while allowing the selective transport of reactants across the mimic barrier. Similar approaches to membrane fabrication include the use of arrays of carbon nanotubes (CNTs). CNTs have been used as membrane structures [5–8] having individual nanotubes that act as synthetic nanopores [9–13], allowing transport parallel to the CNT axis. In contrast, VACNF membranes function by controlling transport perpendicular to the orientation of the nanofibre, relying on interfibre spacing to determine pore size.

The directed assembly [14–17] and controlled growth [18–21] of VACNFs has been well established [22]. VACNFs are compatible with high temperature and chemically aggressive microfabrication techniques [1, 2, 4, 23, 24] and their location can be defined using micro and nanofabrication processes [25, 26]. VACNF membrane structures that are integrated with microfluidic structures or that contain small, cellular scale fluid volumes have been described [2, 3]. It has also been shown that the pore size and chemical properties of the membrane can be altered by techniques that modify the exterior of the nanofibre including plasma enhanced chemical vapour deposition (PECVD) of silicon dioxide.

Characterizing membrane transport characteristics presents significant challenges. Complications include the length of time involved in conducting diffusion experiments and limitations in correlating microscopic membranes with nanoscale behaviour [27]. In previous work, the nanoscale, size-selective transport feature of the VACNF membrane was characterized in a semi-quantitative fashion by allowing multi-sized, fluorescently labelled latex beads to diffuse through the membrane. Subsequently, a bead-size threshold for transport was identified [1–4]. However, the characterization of molecular scale porosity with such nanoscale particle probes is slow ($D \sim 1 \times 10^{-9}$ cm^2 s^{-1}) and requires additional steps to ensure probe suspension. Fluorescence recovery after photobleaching (FRAP) is an ideal technique for meeting the challenge of characterizing transport at the molecular level. For example, FRAP experiments have been conducted to quantify the transport mode in the cytosolic space [28], the plasma membrane [29], organelles [30, 31], and the nucleus [32] of biological cells. Additionally, fluorescent probe diffusion in photosynthetic membranes [33], biological polymers [34], and inorganic, high-aspect ratio colloidal rods [35] have all been studied by FRAP. The FRAP technique is used in this work to determine and quantify the diffusion behaviour for the restricted transport of a small molecule in the presence of a significant fraction of static obstacles (a VACNF forest). The analysis includes the consideration of both excluded volume effects and molecule–nanofibre surface interactions and was able to predict anomalous subdiffusion resulting from the high volume fraction of VACNFs (21–40%) in the stochastic forests.

Anomalous subdiffusion [36–40] transport has been identified as an alternative mode of diffusive transport relative to the classical random walk, Fickian mode. Anomalous subdiffusion most often occurs under the circumstances of either a significant excluded volume in the transport domain [41] and/or active binding/release processes [42–44]. In the instance of binding/release processes, diffusion exhibits alternating periods of arrest and transport, so-called 'Levy-flights' [44].

Random walk in a continuous, isotropic media is described by the Fickian-based expression:

$$\langle r^2 \rangle = 6Dt \tag{1}$$

that relates the linear dependence of mean square displacement $\langle r^2 \rangle$ on time. D is the *time-independent* diffusion coefficient. This expression fails to describe diffusive transport in a disordered media containing a significant fraction of randomly distributed, or a fractal [45–47] distribution, of obstacles. The transport characteristic of the anomalous subdiffusion, obstructed volume model is more appropriately described by the expression:

$$\langle r^2 \rangle = 6\Gamma t^{\alpha} \tag{2}$$

where Γ is a time-independent constant and α is the anomalous subdiffusion exponent. The values of α may range from 0 to 1. Such transport *is characterized by a reduced flux relative to the case of Fickian self-diffusion in an unobstructed solution*. Anomalous subdiffusion that obeys equation [2] as $t \to \infty$ is purely fractal in nature, i.e., across all length and time scales. It is important to note that the anomalous subdiffusion obstructed volume model is but one version of an anomalous diffusion model. Alternatives such as the CTRW [48, 49] and fBm [50–53] models exist.

Theory and modelling have played a key role in quantifying transport in disordered media [36–59]. Several instances of anomalous subdiffusion behaviour have been reported in the literature for a wide range of transport-based phenomenon [60–65]. Moreover, anomalous subdiffusion has been identified for several cases related to solute transport at small scales including the interdiffusion of multiple species in solution [66], the diffusion of a single species in the presence of a significant fraction of static obstacles [67], concentration-dependent diffusion $D(C(t))$ [68, 69], and in complicated environments of proteins diffusing in a macromolecular crowded solution [70, 71]. It is important to note that in these referenced cases the term anomalous does not imply purely anomalous behaviour; in many instances the transport mode is a mix of anomalous and Fickian transport in time. Under this circumstance, it is useful to define a crossover length R_{CR} [41] at which point the transport behaviour changes from anomalous to Fickian. For example, a purely fractal obstructed domain, independent of length scale, would have an $R_{CR} = \infty$. However, for a finite range of self-similarity R_{CR} will have a discrete value and a crossover from anomalous to Fickian transport will be observed.

FRAP measurements were performed in this work using a small molecule, fluorescein isothiocyanate (FITC, hydrodynamic radius 0.54 nm), to characterize the passive, translational diffusive transport property of this small molecule in a VACNF forest. The results were compared to FRAP measurements on the diffusion of FITC in an unobstructed space and oxVACNF forests. Thick SiO_2 conformal coatings were applied to the nanofibre surfaces (oxVACNFs) creating a porous network with a pore diameter <250 nm. Concomitant with this reduction in pore size, transport rates across the membrane were observed to diminish. The flux reduction was attributed to the fact that the oxVACNFs occupy a significant volume in the membrane region that acts to impede diffusive transport through this region. Anomalous subdiffusion was identified as the specific cause for the observed flux reduction based on an analysis with Monte Carlo and finite difference numerical approaches to fit the experimental data. Together these experimental and simulation techniques aid in defining approaches to tailor the transport of molecular sized species through VACNF membranes.

2. Experimental details

2.1. FRAP experiments

A Leica TCS SP2 UV scanning, confocal microscope equipped with a FRAP software package was used to conduct the FRAP experiments and display and export the FRAP data. The 488 nm Ar^+ (50 mW ultraviolet) laser line was used to excite FITC ($C_{21}H_{11}NO_5S$, 389.4 g mol^{-1}, Sigma Chemical Co.) and the subsequent emission was detected in the microscope's xyt scan mode. A Leica PL FL 63×/0.7 corr air objective was used to focus and steer the laser illumination for photobleaching as well as for detecting the sample fluorescence. A tunable acousto-optical beam splitter (AOBS®, Leica) was used to separate the excitation laser line from the emitted molecular fluorescence. A dichroic reflection short pass filter RSP500 was used to split and detect the FITC emission, from the excitation light, over the total detection range of $\lambda = 498$–600 nm. A 100 μM solution of FITC dissolved in a solution of H_2O–20% glycerol ($C_3H_8O_3$, 92.09 g mol^{-1}) was used as the fluorescent species for all experiments. Fluorescence recovery occurs quickly for small molecules such as FITC; 50% intensity recovery occurs on the order of hundreds of microseconds. Therefore, glycerol (20%/v) was added to the fluorescent solution in order to increase the solvent viscosity and to reduce the diffusion coefficient of FITC. The minimum frame acquisition time of 1000 Hz was used to collect the maximum number of data points per unit time; data points were collected with the minimum spacing of $\Delta t = 416$ ms.

Photobleaching illumination was carried out using 16 serial laser pulses of 100% relative intensity to bleach a tetragonal region-of-interest (ROI) geometry with dimensions of $x = 60\ \mu\text{m} \times y = 60\ \mu\text{m} \times z = 12\ \mu\text{m}$. The ROI was discretized into 256 × 256 pixel elements and an electronic zoom factor setting of 8 was used during data collection. The manual, Leica laser power/potentiometer was set to ∼75% of maximum intensity. The illumination intensity was reduced to 2% relative intensity for detecting the fluorescence recovery emission to avoid photobleaching during the recovery cycle.

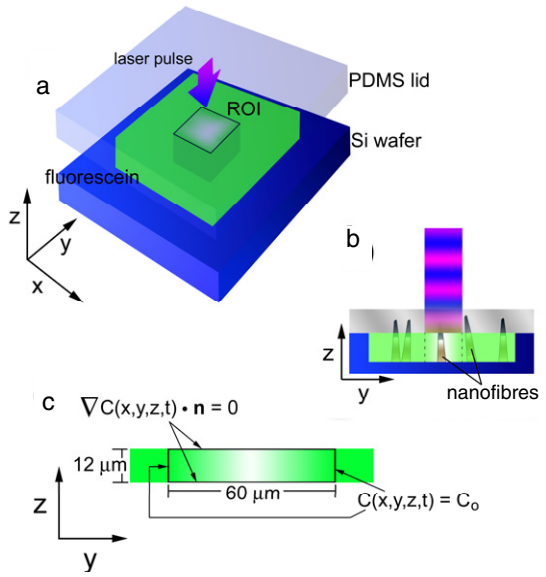

Figure 1. (a) A 3D illustration of the geometry bounding the FRAP region-of-interest (ROI). The Ar^+ ion laser pulse passes through the PDMS lid at normal incidence and bleaches a tetragonal ROI volume down to the Si wafer substrate. (b) The bleached area is bounded by both the PDMS lid and Si wafer substrate in the z-direction while unbleached fluorescein bounds the ROI in the x- and y-directions. (c) The ROI extends the full 12 μm depth of the microfluidic channel in the z-direction and has a square 60 μm × 60 μm shape in the x- and y-directions. A finite difference simulation was created to aid in data interpretation; the boundary conditions for the FRAP simulation are listed in figure 1(c) where Neumann and Dirichlet conditions were used in the z- and x- and y-directions, respectively.

The total ROI intensity was collected as a function of time, in increments of $\Delta t = 416$ ms for fluorescence in an unobstructed environment and $\Delta t = 3.334$ s for a substantially crowded, oxVACNF forest. Experiments were terminated when the fluorescence intensity reached a steady-state value. Correction was made for photobleaching during the recovery cycle by collecting data out to the time of interest without a photobleach pulse cycle. A slight decrease (∼5%) in fluorescence intensity was observed during the fluorescence recovery cycle and the final FRAP data was corrected for this photobleaching.

2.2. VACNF populated microfluidic channel

Figure 1(a) shows a schematic illustration of the sample and substrate used for the FRAP experiment. The laser beam enters the microfluidic structure through a transparent polydimethylsiloxane (PDMS, Sylgard 182 silicone elastomer base, Dow Corning) lid that is used to seal the structure. The FITC is contained within the volume between the PDMS lid and Si substrate. Experiments were conducted for three different cases; in one case the channel is filled with FITC alone while in the two other cases VACNFs and oxVACNFs are present in the channel. The orientation of the nanofibres is vertical with respect to the Si wafer substrate as is illustrated in figure 1(b). The microfluidic channel was formed by a reactive ion etch (RIE) process that anisotropically etched a 2 mm wide, 12 μm deep channel into the Si wafer substrate. Figure 1(b)

shows a cross-sectional illustration through the channel during the laser irradiation step of the ROI. The instance of irradiated fluorescein in the midst of a VACNF forest is illustrated. The ROI is a small volume 4.32×10^4 μm^3 relative to the total volume of the channel 7.8×10^7 μm^3 that ensures a constant concentration of FITC at the ROI boundaries following the photobleach step. Figure 1(c) shows the exact dimensions of the ROI that was shown as an illustration in figure 1(b). A finite difference approach was used to simulate the recovery after photobleaching and the boundary conditions that were used for this simulation are also shown in figure 1(c).

2.3. VACNF growth

The carbon nanofibre forest nucleates and grows from an initially continuous Ni catalyst thin film, 50 nm thick, deposited uniformly over the entire microchannel floor by the electron beam evaporation technique. Ni was deposited only in the microchannels through the use of a photoresist masking layer that coated the Si wafer substrate surface. The VACNF growth process begins by converting the thin, continuous Ni film into a random array of Ni particles by a direct-current (DC) plasma etch (100 mA) in 80 cm^3 min^{-1} NH_3 atmosphere at a total pressure of 3 Torr and an elevated temperature of 700 °C. The combination of etching and annealing leads to the formation of a nanocatalyst film morphology. Carbon nanofibre growth occurs at the discrete nanocatalyst surfaces in response to the introduction of 55 cm^3 min^{-1} C_2H_2 to the NH_3 atmosphere. The acetylene decomposes at the Ni nanocatalyst surface, diffuses to the nanocatalyst–Si interface, and deposits there. The deposition accumulates to form a vertical, carbon nanofibre morphology with an internal structure consisting of tapered graphene sheets. The nanofibres grow in a vertical direction parallel to the electric field lines of the applied field.

The DC–PECVD VACNF growth conditions listed above produced a VACNF forest with an average nanofibre surface density of 4.4 ± 0.3 nanofibres μm^{-2} and an average nanofibre radius of $d = 214 \pm 32$ nm. The 3D occupied volume of the nanofibres in the total microfluidic channel volume was $\phi = 0.21$. These characteristics of the nanofibre forest were determined by analysing several scanning electron microscope images acquired from randomly selected regions throughout the VACNF populated channel. These parameters were changed following the deposition of the SiO_2 conformal nanofibre coating. The surface density of nanofibres changed to 1.0 ± 0.1 nanofibres μm^{-2} and an oxide nanofibre diameter of 1.164 ± 0.22 μm by the deposition of a conformal oxide coating that merged adjacent VACNFs thereby reducing the effective surface density of oxide-coated VACNFs. The occupied volume increased to $\phi = 0.40$ following the deposition of the SiO_2 on the VACNF surfaces.

2.4. SiO_2-coated VACNFs

An Orion thermal PECVD growth chamber manufactured by Trion Technologies was used to apply a thick and uniform, conformal coating of SiO_2 to the VACNF forest in order to increase the occupied volume in the microfluidic device. A total pressure of 1 Torr was established in the growth chamber by flowing a combination of SiH_4 gas at 125 cm^3 min^{-1} and NO_2 also at 125 cm^3 min^{-1}. The substrate temperature was set to 400 °C for a growth time of $t = 800$ s under a plasma power of 25 W. These growth conditions produced a conformal annulus of SiO_2 around the nanofibre surfaces with a thickness of 470 ± 90 nm.

2.5. Simulation and modelling

A 3D finite difference FRAP computer program was created to simulate diffusion into the tetragonal photobleach geometry used in FRAP experiments. In addition, a 3D Monte Carlo-based, non-self-avoiding random walk simulation, carried out in the same tetragonal photobleach geometry, was used to track the individual temporal migration of a collection of bleached particles in the ROI volume as a function of time. The advantage of the Monte Carlo approach for simulating anomalous subdiffusion, relative to the finite difference approach, is that, in the event of both steric and binding interactions during transport, the relative contributions of each may be determined. The finite difference approach provides only a plot of fluorescence recovery in the event of anomalous subdiffusion but converges to an accurate solution more rapidly. The Monte Carlo process was also used to generate an artificial, stochastic VACNF array to mimic real, fabricated VACNF forests by sampling random numbers from the statistical distributions of nanofibre diameter and tilt. Figure 2(a) shows an SEM image of VACNF forest and figure 2(b) shows a computer generated forest using the Monte Carlo approach. Circles superimposed over both the images indicate the presence of nanofibre clusters. The clusters impart a fractal character to the VACNF forest as will be discussed below. The supplementary material section (available from stacks.iop.org/Nano/17/5659) contains a detailed description of both computer simulations. Figure 2(c) shows an SEM image captured at $\theta = 30°$ of a narrow row of VACNFs. FRAP experiments were performed on microfluidic channels completely filled with VACNFs; only a narrow section of VACNFs is shown in figure 2(c) so that the complete, tip-to-base morphology can be observed.

3. Results

3.1. FRAP measurements on FITC in an open channel

Fluorescence recovery curves were analysed by computational data fitting procedures which included both a finite difference, continuum-based approach as well as a Monte Carlo, multiple particle tracking simulation. Figure 3 displays the experimental recovery data for three cases including (1) the control experiment of dilute 0.1 mM FITC diffusing in an unobstructed volume, and (2) FITC diffusion in a VACNF forest and (3) an oxVACNF forest. Superimposed on the figure are the various fits to the recovery curves. For each Monte Carlo data fit, quantitative simulation output includes the calculated apparent diffusion coefficient as a function of time (figure 4) as well as a histogram of the distribution of molecular diffusion coefficients (figure 5).

FRAP experiments were first performed using a 0.1 mM FITC solution contained within a microchannel that was devoid of VACNFs. Figure 3(a) (*black square data points*) shows the cumulative average result of FRAP measurements made at different locations in the nanofibre-free microchannel. The

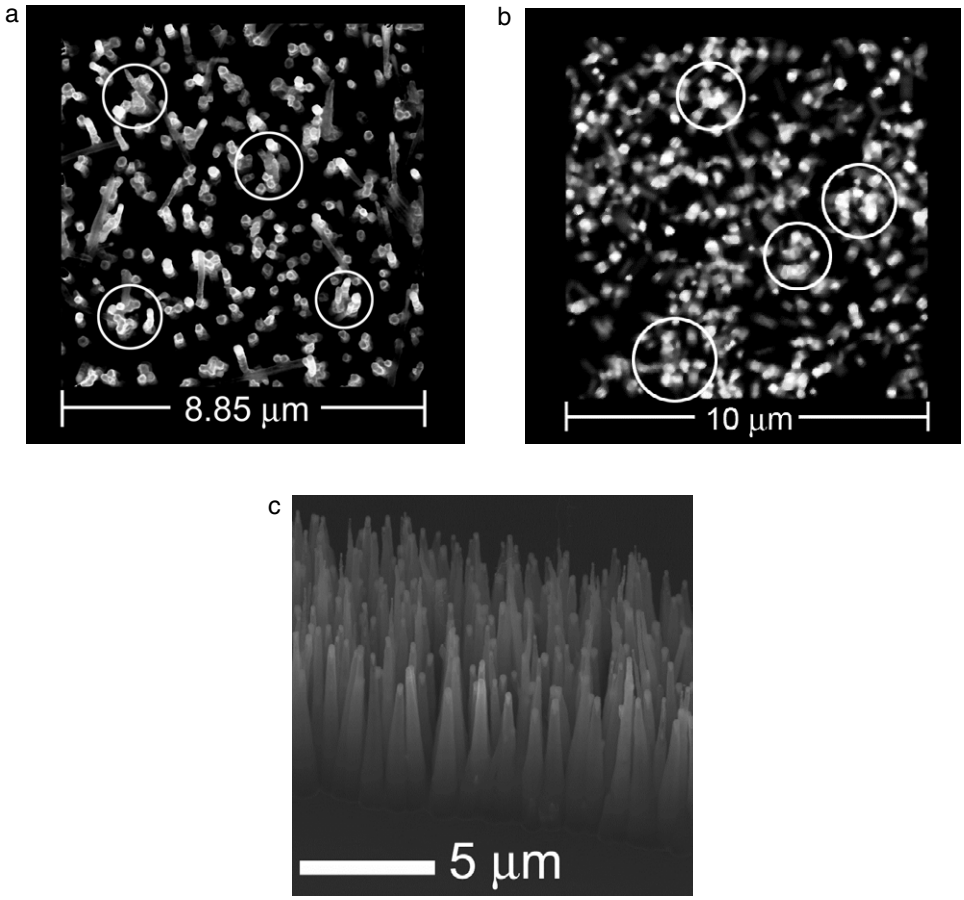

Figure 2. (a) SEM image at normal incidence of a VACNF forest in a Si-microfluidic channel. The VACNF forest has an average nanofibre surface density of 4.4 ± 0.3 nanofibres μm^{-2} and an average nanofibre diameter of 214 ± 32 nm. The 3D occupied volume of the nanofibres is $\phi = 0.21$. The dark space in the image is unoccupied volume and is available for molecular transport. The superimposed circles overlapping the image indicate clusters of nanofibres. (b) A Monte Carlo simulation was used to generate the VACNF forest displayed in this image. The VACNF forest was emulated by random number sampling from the normal, statistical distributions of nanofibre diameter and tilt. These distributions were determined by calculating the statistical distribution (mean and variance) of the relevant nanofibre geometrical parameters from the real, VACNF forest displayed in (a). Note the clustering of VACNFs in the simulated image and their similarity to the observed clustering in the SEM image of the VACNF structure shown in (a). (c) A SEM image of a row of VACNFs taken at $\theta = 30°$ tilt to show the complete morphology of the nanofibres. FRAP experiments were performed on microfluidic channels completely filled with VACNFs; only a section of VACNFs is shown here so that the complete, tip-to-base morphology can be observed.

plot was constructed by first calculating the total intensity in the ROI for each time node $I(t)$ followed by applying the Axelrod [72] normalization procedure to the data. A 3D finite difference simulation was used to fit the data set by solving for the diffusion coefficient D that provides the best fit to the data. The finite element simulation converged to a diffusion coefficient of $D = 3.1 \pm 0.1 \times 10^{-6}$ cm^2 s^{-1}. This value for the diffusion coefficient of FITC in PBS is within 15% of the value of 2.6×10^{-6} cm^2 s^{-1} reported in the literature [32, 66]. Moreover, the calculated diffusion coefficient was independent of time over the extent of the experiment indicating that *Fickian* diffusion was the active transport mode for this experiment.

3.2. FITC diffusion in the VACNF forest

FITC–nanofibre interactions were found to rate-limit molecular transport behaviour beyond $t > 6.8$ s for the case of fluorescence recovery in the VACNF forest; anomalous subdiffusion resulted. Figure 3(b) displays the fluorescence recovery curve for FITC diffusion in a VACNF forest (black triangle data points). This nanofibre population occupies 21% ($\phi = 0.21$) of the total available volume in the microchannel constituting a significantly crowded environment; referenced against published values of volume occupancy [36–39] this value is large enough to expect transport characteristic of anomalous subdiffusion. *Indeed, anomalous subdiffusion was determined to be the operative mode of FITC transport in the inter-nanofibre space as (1) the total flux of unbleached FITC back into the centre of the nanofibre populated ROI was reduced in magnitude relative to the flux of FITC into the same tetragonal ROI volume with* ($\phi = 0$) and (2) the governing, Smoluchowski 3D partial differential equation with a time-independent diffusion coefficient $D \neq f(t)$ proved inadequate to accurately fit the FRAP data (not shown in figure 3).

A Monte Carlo simulation of the VACNF diffusion experiment is shown in figure 3(b) (*grey line*). A first approach to fit the fluorescence recovery data neglecting the FITC–nanofibre interaction was unsuccessful. For example, a correct

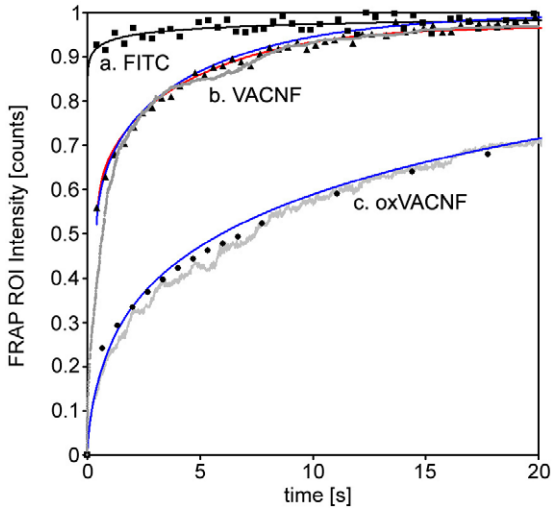

Figure 3. FRAP data for the diffusion of FITC in an obstacle-free ROI (■), a VACNF forest (▲), and in an oxide-coated VACNF (oxVACNF) forest (●). (a) A finite difference simulation fit to the data of uncrowded diffusion yields a constant diffusion coefficient of $D(0 < t \leqslant \infty) = 3.1 \pm 0.1 \times 10^{-6}$ cm^2 s^{-1} for 0.1 mM FITC in PBS. Anomalous subdiffusion was observed for the experiments of FITC diffusion in the (b) VACNF and (c) oxVACNF forest. In order to estimate the time-dependent, apparent diffusion coefficient (figure 4) required fitting the experimental FRAP data using a multiple particle tracking Monte Carlo simulation (grey curves). In addition, finite difference solutions of anomalous subdiffusion are superimposed where $\Gamma = 1.2 \pm 0.1 \times 10^{-6}$ cm^2 s^{-1} and $\alpha = 0.90$ for the VACNF forest and $\Gamma = 1.2 \pm 0.1 \times 10^{-6}$ cm^2 s^{-1} and $\alpha = 0.70$ for the oxVACNF forest (blue curves). The red curve represents the data fit generated by inserting the $D(t)$ versus t output from the Monte Carlo simulation into the finite difference simulation to act as a control for testing the mutual convergence of the two types of simulations. Mutual convergence was observed.

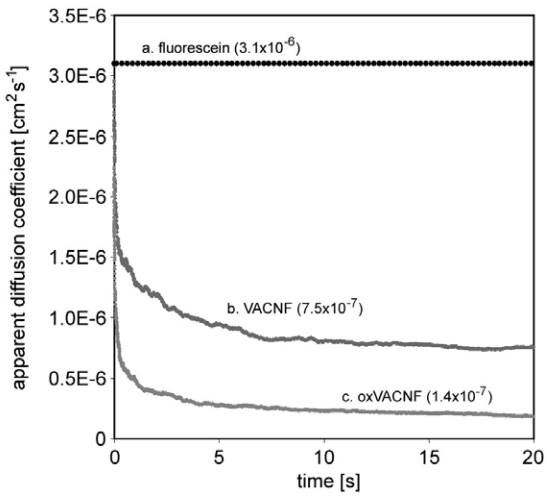

Figure 4. The apparent diffusion coefficient as a function of time extracted from experimental FRAP data by a Monte Carlo data fit for the experiments of (a) FITC diffusion in an unobstructed domain ($D = 3.1 \times 10^{-6}$ cm^2 s^{-1}), (b) in a VACNF forest ($D(t = 16.4\text{ s}) = 7.5 \times 10^{-7}$ cm^2 s^{-1}) and (c) in an oxVANCF forest ($D(t = 17.1\text{ s}) = 1.4 \times 10^{-7}$ cm^2 s^{-1}).

data fit during initial fluorescence recovery $t < t_{0.5}$ (time at which half the bleached intensity has recovered) led to a

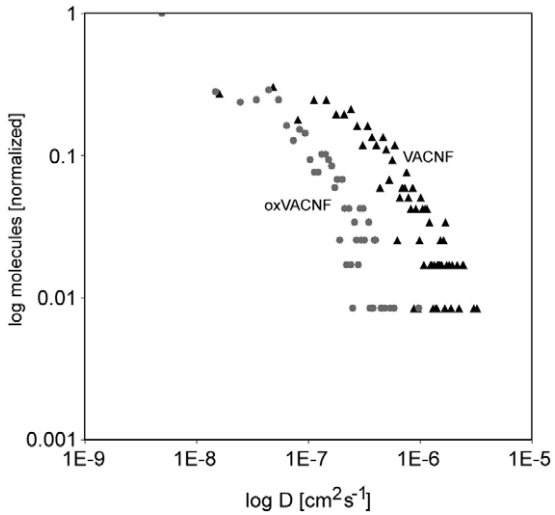

Figure 5. The distribution of molecular diffusion coefficients for anomalous subdiffusion in the VACNF and oxVACNF forest plotted on log–log axes and normalized to the maximum ΔD histogram bin size. The multiple particle tracking method was used to calculate the $D(t)$ for each molecule diffusing in the obstructed inter-nanofibre space. The VACNF forest occupies $\phi = 0.21$ of the transport domain while the oxVACNF domain occupies $\phi = 0.40$ of the available space causing the decrease in the apparent diffusion coefficient distributions to smaller values.

significant over estimation of recovery at long recovery times $t > t_{0.90}$. However, the introduction of a binding interaction into the Monte Carlo simulation, led to a much improved fit to the recovery data. The Monte Carlo data fit represents the average of ×5 computer experiments conducted on ×5 Monte Carlo generated VACNF nanofibre forests. A computer-based search over k_{ads}–k_{des} space (supplementary material available from stacks.iop.org/Nano/17/5659) yielded convergent values of $k_{ads} = 0.15$ s^{-1} and a $k_{des} = 0.18$ s^{-1} to produce the best data fit and is displayed in figure 3(b). These values represent the solution for the case of nanofibre surfaces that were fully saturated with potential binding sites. The binding interaction was found to dominate the fluorescence recovery process over 77% of the total fluorescence recovery time for the VACNF forest (figure 3(b)) and hence accounted for the observed restriction in molecular transport (anomalous subdiffusion) relative to the uncrowded domain (figure 3(a)). Transport following the final photobleach pulse is driven by a phase of rapid diffusive recovery up to $t = 6.8$ s, at which point the binding interaction becomes significant and from this time point forward, controls diffusive transport.

A time-dependent diffusion coefficient (equation (4)) from anomalous diffusion theory was substituted into Smoluchowski's transport equation (equation (3)) in an attempt to model the anomalous fluorescence recovery using the continuum approach. In addition to the Monte Carlo simulation, the finite difference approach also fitted the data accurately and precisely (figure 3(b), blue curve). The finite difference simulation converged to a solution with the values of $\Gamma = 1.2 \pm 0.1 \times 10^{-6}$ cm^2 s^{-1} and an anomalous subdiffusion exponent of $\alpha = 0.90$.

3.3. Controls to confirm simulation results

Finite difference solutions are extremely sensitive to the spatial and temporal increments chosen to discretize the simulation domain. In order to verify the accuracy of convergence of the finite difference FRAP results, the apparent diffusion coefficient versus time data, derived from Monte Carlo simulations (figure 4, below), was used as input into the finite difference simulation for $D(t)$. This should produce a quality fit to the data because the Monte Carlo data fit is of high quality (figure 3(b), grey). Figure 3(b) (red data fit) shows the results of this finite difference solution and indeed, the spatial and temporal discretization of the finite difference matrix was of sufficient resolution to converge to a solution which agrees well with the experimental data and the Monte Carlo simulation.

3.4. FITC diffusion in the oxide-coated (oxVACNF) forest

FRAP experiments were also conducted on oxVACNFs with a crowded volume of $\phi = 0.40$. The additional obstructed volume present in the oxVACNF forest, relative to the VACNF forest, further reduced the flux of bleached FITC out of the ROI volume. Figure 3(c) shows the reduction in fluorescence intensity incurred by measuring transport in the crowded oxVACNFs. *In this case however, the FRAP data was accurately fitted considering only steric effects for altering diffusive transport*. Moreover, fluorescence recovery experiments were conducted on a series of oxVACNF forests of various average nanofibre diameters. The purpose of these experiments was to quantify the reduction in FITC flux as the average VACNF diameter was increased, but also acted as a control to ensure that FITC–VACNF binding interactions remained absent as the average nanofibre diameter changed. This series of recovery curves were fitted by changing only the apparent diffusion coefficient without the need for including a binding interaction in the simulations.

The negligible binding interaction observed for FITC transport in the oxVACNF forest was attributed to the change in surface chemistry of the VACNFs upon coating with SiO_2. Again, the anomalous subdiffusion theory also converged to an accurate solution with values of $\Gamma = 1.2 \pm 0.1 \times 10^{-6}$ cm^2 s^{-1} and $\alpha = 0.70$. A reduction in the anomalous subdiffusion exponent of 22% resulted from the increase by 50% of obstructing nanofibres.

3.5. Apparent diffusion coefficients

The quality of the data fits allowed us to extrapolate quantitative information from the Monte Carlo simulation results as representative of the experimental FRAP data. This information included a plot of the apparent diffusion coefficient as a function of time (figure 4) and a histogram of the distribution of apparent diffusion coefficients as calculated from each particle of the Monte Carlo simulation (figure 5). The time-dependent characteristic of the apparent diffusion coefficient was calculated from a multiple particle tracking subfunction that was embedded within the Monte Carlo, random walk simulation. The ensemble mean square displacement $\langle r^2 \rangle$ is calculated per simulation time step Δt, and through the use of equation [1], the ensemble average diffusion coefficient, or apparent diffusion coefficient, may be calculated. Figure 4 shows the apparent diffusion coefficient versus time for FITC transport in the (b) VACNF and (c) oxVACNF forests and for reference the time-independent diffusion coefficient for FITC in an unobstructed domain (figure 4(a)). The apparent diffusion coefficient saturates at a value of 7.5×10^{-7} cm^2 s^{-1} after $t = 16.4$ s for the VACNF forest. Saturation to steady-state D occurred at $t = 17.1$ s ($D = 1.4 \times 10^{-7}$ cm^2 s^{-1}) for transport in the oxVACNF volume. The histograms shown in figure 5 were created by sorting each molecule based on its D value calculated from (equation (1)) the multiple particle tracking output. The distribution was collected at $t = 16.4$ s for the VACNF forest and at $t = 17.1$ s for the oxVACNF forest. The data was binned into 100 increments over the total time range. Thus, the apparent diffusion coefficient values of $D(t = 16.4\text{ s}) = 7.5 \times 10^{-7}$ cm^2 s^{-1} and $D(t = 17.1\text{ s}) = 1.4 \times 10^{-7}$ cm^2 s^{-1} represent averages of the D data displayed in figure 5. Figure 5 illustrates the importance of the term *apparent diffusion coefficient* as it is an average of a range of individual *molecular diffusion coefficients*.

4. Discussion

4.1. Experimental observation of binding

The Monte Carlo simulation required a binding event, with $k_{ads} = 0.15$ s^{-1} and a $k_{des} = 0.18$ s^{-1}, to provide a smooth fit to the FRAP data for the case of the VACNF forest. Without the binding interaction, the Monte Carlo simulation significantly underestimated the time required for complete fluorescence recovery (by 50%) in the VACNF forest. Moreover, the Monte Carlo simulation fitted the oxVACNF recovery curve considering the steric effect alone which also agreed with experiment; no binding interaction was required. The FITC–VACNF binding may be due to a hydrophobic interaction resulting from π bonding of the aromatic portion of FITC with the predominantly hydrophobic VACNF forest. In solution, FITC (pK_a6.4) [73, 74] carries a negative charge in the pH 7.4 PBS buffer. However, an electrostatic FITC–nanofibre interaction is expected to be negligible due to the high salt concentration in the solution (150 mM NaCl). Moreover, the hydrophobic interaction is more likely considering also the lack of interaction observed between the hydrophobic FITC and the hydrophilic oxVACNFs (a negative charge on FITC may explain why there is no adsorption to oxide-coated fibres).

An additional and relatively stronger binding interaction was also identified for the FITC–VACNF interaction pair. The presence of VACNFs in the FRAP volume was found to *permanently immobilize* a fraction of bleached FITC molecules. Permanent FITC immobilization prevented the full recovery of the post-bleach FRAP intensity to the pre-bleach value. These tethered, non-fluorescent molecules reduced the total volume available for fresh, fluorescent FITC to occupy upon recovery. It was calculated that the fluorescence intensity recovery was reduced by 3.6% in a VACNF populated volume ($\phi = 0.21$) relative to an empty volume. This value corresponds to 7.7×10^7 $C_{21}H_{11}NO_5S$ molecules bleached and bound for the 0.10 mM solution used. On the other hand, immobilized, bleached FITC was not detected in recovery curves for FRAP experiments on

oxVACNFs. Full fluorescence recovery was observed for this case. Hence, the chemical nature of the uncoated VACNF surface also favoured, in addition to the weaker hydrophobic interaction, a relatively stronger binding interaction with the FITC molecule.

4.2. Anomalous and Fickian transport in the VACNF forest

The molecular diffusion of irradiated, bleached FITC ensues immediately following the photobleach pulse according to the time-independent diffusion coefficient of FITC (3.1×10^{-6} cm^2 s^{-1}). This Fickian mode of transport is independent of time until individual molecules encounter the nearest nanofibre to their initial location. The first nanofibre interaction takes place, on average, at $t = 0.1$ ms; the time required for a molecule to travel a distance equal to the average nanofibre spacing by Brownian motion. Anomalous subdiffusion ensues either by FITC binding to the nanofibre surface (VACNFs) or by steric obstruction (oxVACNFs). The diffusion coefficient then transitions to a time-dependent variable. As individual molecules interact with an increasing number of nanofibres, the apparent diffusion coefficient decreases (figures 4(b) and (c)) *but also at a decreasing rate*, as the collective nanofibre medium begins to appear more like an isotropic distribution of obstacles to the collection of diffusing particles. A simple analogy follows to explain this concept more clearly. The reader could imagine holding the SEM image in figure 2(a) very close to the eye such that only an individual nanofibre is in view. Certainly the portion of the image in the field of view is not a very homogeneous medium. This field of view represents the area of space explored by a molecule executing Brownian motion over a short time period, equivalent in distance to the inter-nanofibre distance. If the reader now moves the image away from the eye such that a greater field of view reveals more of the SEM image, the collection of randomly distributed VACNFs now appears more isotropic than before, i.e., the medium of obstacles is approaching a more uniform distribution. Moving the page away from the eye is analogous to advancing time; more time is required for a molecule to walk this space. Eventually, the image will reach a sufficient distance from the eye such that the level of visual homogeneity saturates. The result of this exercise is an asymptotic approach of the apparent, time-dependent diffusion coefficient to a steady-state, Fickian value.

4.3. The extent of the anomalous diffusion regime

Anomalous subdiffusion theory attributes the nonlinear transport in a disordered media to the random or fractal nature of the crowding medium [36–41]. It was found that the Monte Carlo approach of randomly placing nanofibres to generate the VACNF forest was mimicked well by a self-similar fractal pattern generated by randomizing a square obstruction, Sierpenski carpet fractal [47, 75] of similar total occupied surface area as the VACNF forest. The fractal-based, residual area-resolved trema Richardson analysis technique [47] was used to quantify in more detail the exact cluster size range over which the fractal character is observed for the VACNF forest. Remarkably, the VACNF forest shown in figures 2(a) and (b) yielded a Sierpenski fractal dimension of $\delta_s = 1.885$; a value within 1% of that calculated for a Sierpenski carpet formed from randomized, square obstructions of similar total occupied surface area ($\phi = 0.21$) [47]. From this fractal dimension was estimated the effective radius of obstacles 189 nm $\leqslant r \leqslant$ 423 nm, i.e., length scale, over which the fractal character was observed. The clusters observed in the SEM image in figure 2(a) fall within this size range. This fractal character arises from (1) the variable diameter of the nanofibres and (2) the clustering of nanofibres. These *clusters of nanofibres act collectively as larger, static obstacles of the same circular geometry as the nanofibres that compose them, i.e., a self-similar fractal pattern exists in the VACNF forest, but only over a very limited length scale*.

In the case of the VACNF forest, $D(t = 16.4\ \text{s}) = 7.5 \times 10^{-7}$ cm^2 s^{-1} is the steady-state, saturated value of the apparent diffusion coefficient D_∞. The average, linear distance $r_{a\to b}$ travelled by the collection of virtual particles at the time of diffusion coefficient saturation to the steady-state, anomalous diffusion coefficient D_∞ is 4.5 μm; $r_{a\to b} = 3.4$ μm for the oxVACNF domain and these values represent the transition from anomalous to Fickian diffusion, i.e., $r_{a\to b} = R_{CR}$ the crossover length described in the introduction section. The value of R_{CR} was less in magnitude in the oxVACNF forest because of the increased number of collisions owing to the larger oxVACNF occupied volume. These values are important quantitative parameters when considering the VACNFs as potential membrane barriers and/or crowding features.

The observed transition from anomalous to Fickian transport has ramifications for using the VACNFs as membrane barriers. The flux across the membrane according to Fick's first law

$$J(x, y) = -D(t) \bullet \nabla \cdot C(x, y) \tag{3}$$

is linearly proportional to the diffusion coefficient. The results presented here reveal an approach to tailor the apparent diffusion coefficient $D(t)$ of molecular sized species in a VACNF forest matrix by changing the interVANCF pore size by conformally coating the fibres with oxide. *Moreover, by changing the width of the membrane the nature of the diffusive transport within the membrane may be tailored as well*. For example, if the membrane width is less than R_{CR} the permeability P,

$$P = \frac{D}{\lambda} \tag{4}$$

where $D(t)$ is the apparent diffusion coefficient and λ is the membrane width, will scale nonlinearly with width as $\lambda(D)$ (figure 4). However, if the membrane is wider than R_{CR} the permeability will again be linear with λ as D is independent of time. The anomalous subdiffusion phenomenon thus provides a means to tailor the membrane flux by engineering membrane width, nanofibre density, and nanofibre surface chemistry.

5. Conclusions

The diffusion of a small, fluorescent molecule (FITC, hydrodynamic radius 0.54 nm) through a VACNF forest was characterized by the FRAP technique. A three-dimensional finite difference simulation for solving Smolukoski's equation was written to fit the FRAP data for the purpose of extracting the apparent diffusion coefficient from the data. Anomalous subdiffusion of FITC in the VACNF forest was

observed, which required that the equation for time-dependent diffusion be added to the finite difference simulation to fit the FRAP data. This approach fitted the data well. However, determination of the exact cause of the anomalous subdiffusion, e.g., molecule–nanofibre interactions or steric effects, required the creation of a multiple-particle-tracking, Monte Carlo simulation where the dual contributions of these interactions could be decoupled in the simulation. Anomalous subdiffusion was attributed to a FITC–nanofibre interaction for the case of diffusion through the VACNF forest. Volume crowding was identified as the cause of anomalous subdiffusion in the oxVACNF forest. The stochastic nature of the VACNF forest also required a Monte Carlo simulation to generate a computer mimic from SEM images of VACNF forests for virtual particles to walk on. In addition to accurately fitting the data, use of the Monte Carlo approach made it possible to determine the nature of the anomalous transport. The apparent diffusion coefficient as a function of time as well as the distribution of molecular diffusion coefficients were extracted data from the simulation.

Both anomalous and Fickian modes of transport were observed for the case of FITC diffusing in the inter-nanofibre space of a VACNF forest. Anomalous, time-dependent diffusion was observed up to a crossover length (R_{CR}) of $R_{CR} = 4.5\ \mu$m for VACNFs and $R_{CR} = 3.4\ \mu$m for SiO_2-coated VACNFs (oxVACNFs). The conformal SiO_2 coating proved a successful approach to reduce inter-nanofibre pore size, increase the occupied volume in the crowded VACNF forest, and change the chemical nature of the VACNF surface. The steric crowding effect in the oxVACNF forest successfully reduced the molecular flux. Beyond the R_{CR}, diffusion saturated to a time-independent, Fickian value for diffusion D_∞ in both VACNF and oxVACNF forests. However, the apparent diffusion coefficient of D_∞ ($t = 16.1$ s) $= 7.5 \times 10^{-7}$ cm^2 s^{-1} for the VACNF forest was significantly higher than the value of $D_\infty(t = 17.1\ \text{s}) = 1.4 \times 10^{-7}$ cm^2 s^{-1} for the oxVACNF forest. The flux through the oxVACNF was significantly reduced. This demonstration of porosity control is a crucial step for designing a membrane tailored for tasks such as controlled release or size-selective transport.

Acknowledgments

This research was supported by NIH Grant EB000657 and a portion of this research was conducted at the Center for Nanophase Materials Sciences, which is sponsored at Oak Ridge National Laboratory by the Division of Scientific User Facilities, US Department of Energy. AVM and MLS acknowledge support from the Material Sciences and Engineering Division Program of the DOE Office of Science. This work was performed at the Oak Ridge National Laboratory, managed by UT-Battelle, LLC, for the US DOE under Contract No. DE-AC05-00OR22725.

This manuscript has been authorized by a contractor of the US Government under contract DE-AC05-00OR22725. Accordingly, the US Government retains a nonexclusive, royalty-free license to publish or reproduce the published form of this contribution, or allow others to do so, for US Government purposes.

References

[1] Zhang L, Melechko A V, Merkulov V I, Guillorn M A, Simpson M L, Lowndes D H and Doktycz M J 2002 *Appl. Phys. Lett.* **81** 135
[2] Fletcher B L, Hullander E D, Melechko A V, McKnight T E, Klein K L, Hensley D K, Morrell J L, Simpson M L and Doktycz M J 2004 *Nano Lett.* **4** 1809
[3] Fowlkes J D, Fletcher B L, Hullander E D, Klein K L, Hensley D K, Melechko A V, Simpson M L and Doktycz M J 2005 *Nanotechnology* **16** 3101
[4] Hullander E D 2006 *IEEE Trans. Nanotechnol.* submitted
[5] Yeh I-C and Hummer G 2004 *Proc. Natl Acad. Sci.* **101** 12177
[6] Holt J K, Noy A, Huser T, Eaglesham D and Bakajin O 2004 *Nano Lett.* **4** 2245
[7] Sun L and Cooks R M 2000 *J. Am. Chem. Soc.* **122** 12340
[8] Dubbeldam D, Beerdsen E, Calero S and Smit B 2005 *Proc. Natl Acad. Sci.* **102** 12317
[9] Sun L and Cooks R M 1999 *Langmuir* **15** 738
[10] Ho C, Qiao R, Heng J B, Chatterjee A, Timp R J, Aluru N R and Timp G 2005 *Proc. Natl Acad. Soc.* **102** 10445
[11] Yang H-H, Zhang S-Q, Yang W, Chen X-L, Zhuang Z-X, Xu J-G and Wang X-R 2004 *J. Am. Chem. Soc.* **126** 4054
[12] Kohli P, Harrell C C, Cao Z, Gasparac R, Tan W and Martin C R 2004 *Science* **305** 984
[13] Hinds B J, Chopra N, Rantell T, Andrews R, Gavalas V and Bachas L G 2004 *Science* **303** 62
[14] Merkulov V I, Lowndes D H, Wei Y Y, Eres G and Voelkl E 2000 *Appl. Phys. Lett.* **76** 3555
[15] Merkulov V I, Melechko A V, Guillorn M A, Lowndes D H and Simpson M L 2002 *Appl. Phys. Lett.* **80** 476
[16] Melechko A V, McKnight T E, Hensley D K, Guillorn M A, Borisevich A Y, Merkulov V I, Lowndes D H and Simpson M L 2003 *Nanotechnology* **14** 1029
[17] Merkulov I A, Melechko A V, Wells J C, Cui H, Merkulov V I, Simpson M L and Lowndes D H 2005 *Phys. Rev.* B **71** 45409
[18] Merkulov V I, Hensley D K, Melechko A V, Guillorn M A, Lowndes D H and Simpson M L 2002 *J. Phys. Chem.* B **106** 10570
[19] Melechko A V, Merkulov V I, Lowndes D H, Guillornn M A and Simpson M L 2002 *Chem. Phys. Lett.* **356** 527
[20] Fowlkes J D, Melechko A V, Klein K L, Rack P D, Smith D A, Hensley D K, Doktycz M J and Simpson M L 2006 *Carbon* **44** 1503
[21] Merkulov V I, Melechko A V, Guillorn M A, Lowndes D H and Simpson M L 2001 *Appl. Phys. Lett.* **79** 2970
[22] Melechko A V, Merkulov V I, McKnight T E, Guillorn M A, Klein K L, Lowndes D H and Simpson M L 2005 *Appl. Phys. Rev.* **97** 41301
[23] Guillorn M A, McKnight T E, Melechko A V, Merkulov V, I, Britt P F, Austin D W, Lowndes D H and Simpson M L 2002 *J. Appl. Phys.* **91** 3824
[24] McKnight T E, Melechko A V, Griffin G D, Guillorn M A, Merkulov V I, Serna F, Hensley D K, Doktycz M J, Lowndes D H and Simpson M L 2003 *Nanotechnology* **14** 551
[25] Guillorn M A, Melechko A V, Merkulov V I, Hensley D K and Simpson M L 2002 *Appl. Phys. Lett.* **81** 3660
[26] McKnight T E, Melechko A V, Hensley D K, Mann D G J, Griffin G D and Simpson M L 2004 *Nano Lett.* **4** 1213
[27] Carbonaro A, Walczak R, Calderale P M and Ferrari M 2004 *J. Membr. Sci.* **241** 249
[28] Dayel M J, Hom E F Y and Verkman A S 1999 *Biophys. J.* **76** 2843
[29] Umenshi F, Verbavatz J-M and Verkman A S 2000 *Biophys. J.* **78** 1024
[30] Sbalzarini I F, Mezzacasa A, Helenius A and Koumoutsakos P 2005 *Biophys. J.* **89** 1482

[31] Olvecsky B P and Verkman A S 1998 *Biophys. J* **74** 2722
[32] Seksek O, Biwersi J and Verkman A S 1997 *J. Cell Biol.* **138** 131
[33] Mullineuax C W and Sarcina M 2002 *Trends Plant Sci.* **7** 237
[34] Gribbon P and Hardingham T E 1998 *Biophys. J.* **75** 1032
[35] van Bruggen M P B, Lekkerkerker H N W, Maret G and Dhont J K G 1998 *Phys. Rev.* E **58** 7668
[36] Havlin S and Ben-Avraham P 1987 *Adv. Phys.* **36** 695
[37] Coppens M-O and Froment G F 1995 *Chem. Eng. Sci.* **50** 1013
[38] Saxton M J and Jacobson K 1997 *Annu. Rev. Biophys. Biomol. Struct.* **26** 373
[39] Grzywna J 1996 *Chem. Eng. Sci.* **51** 4115
[40] Martin D S, Forstner M B and Kas J A 2002 *Biophys. J.* **83** 2109
[41] Saxton M J 1994 *Biophys. J.* **66** 394
[42] Saxton M J 1996 *Biophys. J.* **70** 1250
[43] Sprague B L and McNally J G 2005 *Trends Cell Biol.* **15** 85
[44] Levy P 1965 *Processus Stochastiques et Mouvement Brownien* (Paris: Gauthier–Villars)
[45] Bouchaud J and Georges A 1990 *Phys. Rep.* **195** 127
[46] Bunde A and Havlin S 1991 *Percolation II. Fractals and Disordered Systems* 2nd edn (Berlin: Springer) pp 96–149
[47] Kaye B H 1989 *A Random Walk through Fractal Dimensions* 1st edn (Weinheim: VCH) pp 13–124
[48] Scher H, Shlesinger M F and Bendler J T 1991 *Phys. Today* **44** 26
[49] Nagle J F 1992 *Biophys. J.* **63** 366
[50] Netz P A and Dorfmuller T 1997 *J. Chem. Phys.* **107** 9221
[51] Lundahl T, Ohley W J, Kay S M and Siffert R 1996 *IEEE Trans. Med. Imaging* **5** 152
[52] Falconer K J and Vehel J L 2000 *Proc. R. Soc.* A **456** 2153
[53] Metzler R and Klafter J 2000 *Phys. Rep.* **339** 1
[54] Leitner D M, Brown F L H and Wilson K R 2000 *Biophys. J.* **78** 125
[55] Johansson L and Lofroth J-E 1993 *J. Chem. Phys.* **98** 7471
[56] Chang R, Jagannathan K and Yethiraj A 2004 *Phys. Rev.* E **69** 051101
[57] Braeckmans K, Peeters L, Sanders N N, De Smedt S C and Demeester J 2003 *Biophys. J.* **85** 2240
[58] Sniekers Y H and van Donkelaar C C 2005 *Biophys. J.* **89** 1302
[59] Karayiannis N Ch, Mavrantzas V G and Theodorou D N 2001 *Chem. Eng. Sci.* **56** 2789
[60] Kirchner J W, Feng X and Neal C 2000 *Nature* **403** 524
[61] Tang Q and Edidin M 2003 *Biophys. J.* **84** 400
[62] Cheng Y, Prud'homme R K and Thomas J L 2002 *Macromolecules* **35** 8111
[63] Kuntz M and Lavellee P 2003 *J. Phys. D: Appl. Phys.* **36** 1135
[64] Dwyer J D and Bloomfield V A 1993 *Biophys. J.* **65** 1810
[65] Mei E, Sharonov A, Gao F, Ferris J H and Hochstrasser R M 2004 *J. Phys. Chem.* A **108** 7339
[66] Periasamy N and Verkman A S 1998 *Biophys. J.* **75** 557
[67] Netz P A and Dorfmuller T 1995 *J. Chem. Phys.* **103** 9074
[68] Kuntz M and Lavallee P 2004 *J. Appl. Phys.* D **37** L5
[69] Kuntz M and Lavallee P 2003 *J. Phys. D: Appl. Phys.* **36** 1135
[70] Banks D S and Fradin C 2005 *Biophys. J.* **89** 2960
[71] Dwyer J D and Bloomfield V A 1993 *Biophys. J.* **65** 1810
[72] Axelrod D, Koppel D E, Schlessinger J, Elson E and Webb W W 1976 *Biophys. J.* **16** 1055
[73] Leonardt H, Gordon L and Livingston R 1971 *J. Phys. Chem.* **75** 245
[74] Highsmith S 1986 *Biochemistry* **25** 1049
[75] Hullander E D 2005 Biomimetic membranes realized with arrays of carbon nanofibers *Thesis*